

RELATIVISTIC MAGNETOHYDRODYNAMICS WITH APPLICATION TO GAMMA-RAY BURST
OUTFLOWS: II. SEMIANALYTIC SUPER-ALFVÉNIC SOLUTIONS

NEKTARIOΣ VLAHAKIS AND ARIEH KÖNIGL

Department of Astronomy & Astrophysics and Enrico Fermi Institute, University of Chicago, 5640 S. Ellis Ave., Chicago, IL
60637

vlahakis@jets.uchicago.edu, arieh@jets.uchicago.edu

Submitted to ApJ on March 19, 2003

ABSTRACT

We present exact radially self-similar solutions of special-relativistic magnetohydrodynamics representing “hot” super-Alfvénic outflows from strongly magnetized, rotating compact objects. We argue that such outflows can plausibly arise in gamma-ray burst (GRB) sources and demonstrate that, just as in the case of the trans-Alfvénic flows considered in the companion paper, they can attain Lorentz factors that correspond to a rough equipartition between the Poynting and kinetic-energy fluxes and become cylindrically collimated on scales compatible with GRB observations. As in the trans-Alfvénic case, the initial acceleration is thermal, but, in contrast to the solutions presented in Paper I, part of the enthalpy flux is transformed into Poynting flux during this phase. The subsequent, magnetically dominated acceleration can be significantly less rapid than in trans-Alfvénic flows.

Subject headings: galaxies: jets — gamma rays: bursts — ISM: jets and outflows — MHD —methods: analytical — relativity

1. INTRODUCTION

In the companion paper (Vlahakis & Königl 2003, hereafter Paper I) we presented a general formulation of special-relativistic magnetohydrodynamics (MHD) and derived exact radially self-similar solutions for axisymmetric outflows from strongly magnetized, rotating compact objects.¹ We pointed out that our results should be relevant to relativistic-jet sources in a variety of astrophysical settings (including miniquasars and active galactic nuclei), but our main focus has been on gamma-ray burst (GRB) outflows.

In Paper I we concentrated on trans-Alfvénic solutions, in which the poloidal magnetic field component dominates (or at least is not much smaller than) the azimuthal field component at the base of the outflow. In the present paper we consider outflows in which $|B_\phi/B_p| \gg 1$ at the origin. The poloidal component of the Alfvén velocity in these flows is very small from the start, and consequently they are effectively super-Alfvénic throughout.² This property of the flows is demonstrated more formally in §2. Contopoulos (1995) discussed nonrelativistic, “cold” outflows of this type in the case where $B_p = 0$ and $B_\phi \neq 0$. Here we study super-Alfvénic outflows in the relativistic limit, taking into account thermal-pressure effects and allowing for the presence of a finite poloidal field component (which is required for angular-momentum transport by the flow).

As in Paper I and in Vlahakis & Königl (2001), we consider a debris disk around a black hole with a massive-star progenitor as a specific example of a long-duration GRB source. If the outflow emanates from a region of characteristic cylindrical radius ϖ_i and radial width $(\Delta\varpi)_i$ (where the subscript i denotes quantities evaluated at the disk surface), and if the disk injects energy into the flow mostly in the form of a Poynting flux over a time interval Δt , then the total injected energy (from the two surfaces of the disk) is

$$\mathcal{E}_i \approx c E_i B_\phi i \varpi_i (\Delta\varpi)_i \Delta t, \quad (1)$$

¹ In this paper we continue to use the notation of Paper I; we identify equations, sections, and figures from that paper by placing the numeral I in front of their respective numbers.

² The tendency of the Alfvén point in trans-Alfvénic outflows to move close to the disk surface when the value of $|B_p/B_\phi|$ at the base of the flow decreases below ~ 1 was illustrated (in the nonrelativistic context) by Cao & Spruit (1994).

where $E = B_p V_\phi/c - B_\phi V_p/c$ is the electric field amplitude. In the trans-Alfvénic case $E \approx B_p V_\phi/c$, and one infers

$$B_{pi} \approx 3 \times 10^{14} \left[\left(\frac{\mathcal{E}_i}{10^{52} \text{ ergs}} \right) \left(\frac{\varpi_i}{1.6 \times 10^6 \text{ cm}} \right)^{-2} \left(\frac{\varpi_i}{2(\Delta\varpi)_i} \right) \times \left(\frac{V_{\phi i}}{10^{10} \text{ cm s}^{-1}} \right)^{-1} \left(\frac{\Delta t}{10 \text{ s}} \right)^{-1} \left(\frac{B_{pi}}{|B_{\phi i}|} \right) \right]^{1/2} G, \quad (2)$$

where the factor $(B_{pi}/|B_{\phi i}|)$ on the right-hand side is typically $\gtrsim 1$ for trans-Alfvénic flows.

A massive star could give rise to a black-hole/debris-disk system in at least three ways: (1) a prompt (within ~ 1 s of core collapse) formation in which no supernova shock is produced (the “Type I collapsar” scenario; e.g., MacFadyen & Woosley 1999); (2) a delayed (within 30–3000 s of core collapse) formation resulting from fallback in a failed supernova explosion (the “Type II collapsar” scenario; e.g., Fryer 1999); (3) a strongly delayed (by a period of weeks to years) formation resulting from the collapse (following the loss of rotational support through a pulsar wind) of a rapidly rotating, massive neutron star created in a successful supernova explosion (the “supernova” scenario; e.g., Vietri & Stella 1998). In the latter scenario, the initial magnitude of B_p in the debris disk would not exceed typical radio-pulsar values ($\sim 10^{12} - 10^{13} G$), and in the Type I collapsar picture the magnitude of an inward-adverted large-scale poloidal field would likely be even lower. In the Type II collapsar scenario it is in principle possible for a strong poloidal field to develop on the scale of the stalled supernova shock on account of either convection (e.g., Thompson & Murray 2001) or a hydromagnetic instability (e.g., Akiyama et al. 2003), but the ability of these mechanisms to produce ordered disk poloidal fields of the required magnitude remains questionable. In any case, most of the long-duration GRBs observed to date are interpreted in the collapsar picture as being of the Type I variety (MacFadyen, Woosley, & Heger 2001).

The most promising mechanism of creating strong fields in debris disks is through shear amplification of the seed poloidal field by the strong (Keplerian) differential rotation (e.g., Mészáros & Rees 1997). This process generates azimuthal fields that can greatly exceed the poloidal field component inside the disk. Klužniak & Ruderman (1998) and Ruderman, Tao, & Klužniak (2000), who considered this mechanism in the contexts of both a debris disk and a newly formed neutron star, suggested that the wound-up field would rise buoyantly but not necessarily axisymmetrically and could emerge from the disk (or stellar) surface as a flux rope with $|B_{pi}|$ of order the amplified $|B_\phi|$. A similar scenario has been proposed for the formation of active regions in the sun and has been tested by numerical simulations (e.g., Brummell, Cline, & Cattaneo 2002; Abbott & Fisher 2003). Klužniak & Ruderman (1998) and Ruderman et al. (2000) also suggested that repeated episodes of field windup and escape could be the origin of the observed intrinsic GRB variability (see § I.4.1.1).

Klužniak & Ruderman (1998) pointed out that an alternative outcome of the field winding process might be the escape of disconnected (through magnetic reconnection) toroidal flux loops. In this case $|B_{\phi i}/B_{pi}|$ could be $\gg 1$. This is similar to the “plasma gun” scenario proposed by Contopoulos (1995). Shibata, Tajima, & Matsumoto (1990) argued, on the basis of numerical simulations, that this behavior is likely to occur explosively and could be manifested by disks in which the pressure of the amplified field increases above the thermal pressure (see also Haswell, Tajima, & Sakai 1992 and Chakrabarti & D’Silva 1994). It is interesting to note that the field windup and reconnection cycle underlying these models was also at the basis of early models of disk magnetic viscosity (e.g., Eardley & Lightman 1975; Coroniti 1981; Stella & Rosner 1984). More recent disk-viscosity models have been based on MHD turbulence induced by the magnetorotational instability (MRI; e.g., Balbus & Hawley 1998). The debris disks invoked in GRB source models are envisioned to be initially threaded by a subthermal poloidal magnetic field, which could make them susceptible to this instability. One might then wonder whether most of the energy liberated in the disk would be viscously dissipated into heat, with little left to power Poynting flux-dominated outflows. Although a definitive answer to this question would entail a fully global numerical investigation of the nonlinear development of the MRI, existing (radially localized) simulations (e.g., Miller & Stone 2000) indicate that disks threaded initially by a weak poloidal field with a nonvanishing mean evolve into configurations that are magnetically dominated throughout (and thus no longer MRI-unstable).

In this paper we explore the possibility that at least some GRB outflows are produced with $|B_{\phi i}/B_{pi}| \gg 1$. In this case $E \approx -B_\phi V_p/c$, and equation (1) implies

$$|B_{\phi i}| \approx 3 \times 10^{14} \left[\left(\frac{\mathcal{E}_i}{10^{52} \text{ ergs}} \right) \left(\frac{\varpi_i}{1.6 \times 10^6 \text{ cm}} \right)^{-2} \left(\frac{\varpi_i}{2(\Delta\varpi)_i} \right) \right. \\ \left. \times \left(\frac{V_{pi}}{10^{10} \text{ cm s}^{-1}} \right)^{-1} \left(\frac{\Delta t}{10 \text{ s}} \right)^{-1} \right]^{1/2} G, \quad (3)$$

where V_{pi} is estimated to be of the order of the speed of sound ($\sim c/\sqrt{3}$) at the base of the flow. Although the behavior of $B_{\phi i}$

³ The implied inequality $\varpi\Omega > c$ is another manifestation of the fact that the region where $B_p \ll -B_\phi$ is located downstream from the “light cylinder,” and hence is super-Alfvénic.

⁴ For $V_{pi} \ll c$, corresponding to $E \ll -B_\phi$, we obtain nonrelativistic solutions, which resemble the ones found by Contopoulos (1995).

⁵ Their force-free formulation enabled them to also include the oppositely-directed [$\propto g(ct + \ell)$] wave, which, however, is γ^2 times weaker than the outgoing one.

in the field-windup scenario is inherently nonsteady, it can nevertheless be incorporated into the quasi-steady “frozen pulse” formalism presented in Paper I, as we proved in § I.2.1.

A brief overview of the application of the r self-similar model outlined in Paper I to super-Alfvénic flows is given in § 2. We present representative “hot” and “cold” solutions in § 3 and discuss analytic approximations to our results in § 4. Our conclusions are summarized in § 5.

2. OUTFLOW DESCRIPTION

As in Paper I, we consider a multiple-shell outflow consisting of baryonic matter, electrons (that neutralize the protons), e^\pm pairs in thermodynamic equilibrium with photons, and a large-scale electromagnetic field. We utilize the r self-similar, ideal-MHD model described in § I.3. Adopting as typical values $|B_{\phi i}| \approx 3 \times 10^{14} G$ and $B_{pi} \approx 3 \times 10^{12} G$, we have $x = E/B_p \approx -B_\phi V_p/cB_p \approx 60 \gg 1$ at the base of the flow, so the condition $M^2 + x^2 > 1$ for super-Alfvénic flows (see § I.3.2.1) is satisfied. In fact, for typical parameters the “Alfvénic” Mach number M (eq. [I.15]) is also $\gg 1$ at the base of the flow, which further sharpens the above inequality.

From equation (I.9) $V_\phi = \varpi\Omega - V_p(-B_\phi/B_p)$. At the base of a trans-Alfvénic flow $B_p \gtrsim -B_\phi$ and hence $\Omega \approx V_\phi/\varpi$. However, when $B_p \ll -B_\phi$, the last term on the right-hand side of the expression for V_ϕ is $\gg c$, so the first term on the same side must also be $\gg c$ in order for their difference to remain $< c$.³ This implies that $\Omega \approx -B_\phi V_p/(\varpi B_p) \gg V_\phi/\varpi$ at the base of a super-Alfvénic flow. In contrast to the trans-Alfvénic situation, in this case the fieldline constant Ω cannot be identified with the matter angular velocity at the footpoint of the fieldline at the midplane of the disk. As was already remarked upon by Contopoulos (1995), the fieldline angular velocity Ω is generally not a meaningful material property. We prefer instead to interpret it in terms of the electric potential Φ : $\mathbf{E} = -(\Omega/c)\nabla_s A = -(1/c)\nabla_s \Phi$, so $\Omega \equiv (\partial/\partial A)\Phi(A, s)$.

In super-Alfvénic flows, $E \approx -B_\phi V_p/c \approx -B_\phi$ everywhere above the disk. This means that the transfield components of the electric and magnetic forces are comparable, $\mathbf{f}_{E\perp} \approx -\mathbf{f}_{B\perp}$. This, in turn, is conducive to a successful evolution of the outflow, as the strong magnetic collimation that tends to pinch the flow is countered by the decollimating electric force, which allows the jet to reach large distances.⁴

The expressions for the various physical quantities that appear in the r self-similar model can be simplified by taking account of the inequalities $M^2 \gg 1 - x^2$ and $x \gg x_A$, which apply in the super-Alfvénic regime. We present the results in Appendix A, showing explicitly the dependences on r , θ , and s . For example, the expression for B_ϕ has the form

$$B_\phi = \underbrace{C}_{\text{const}} \times \underbrace{r^{F-2}}_r \times \underbrace{\frac{(\sin\theta)^{F-2}}{\mathcal{X}^{F-3}(\mathcal{X}^2 + M^2)}}_\theta \times \underbrace{[g(ct - \ell)]^{1/2}}_{s=ct - \ell}.$$

Because of the s dependence, the outflow looks like an outward-propagating wave, which is the generalization of the electromagnetic outflows (ignoring inertia) described by Lyutikov & Blandford (2002).⁵ The unknown functions of θ can be obtained after integrating the ordinary differential equations

TABLE 1
PARAMETERS OF REPRESENTATIVE SOLUTIONS[†]

solution	F	$\theta_i(^{\circ})$	Θ_i	$\rho_{0i}(\text{g cm}^{-3})$	$B_{pi}(\text{G})$	$B_{\phi i}(\text{G})$	$\vartheta_i(^{\circ})$	V_{pi}/c	$V_{\phi i}/c$
<i>a</i>	1.01	85	0.7685	726	1.2×10^{12}	-1.2×10^{14}	60	0.7627	0.5
<i>b</i>	1.01	85	0.011	437	1.2×10^{12}	-1.2×10^{14}	60	0.7737	0.5

[†] In both cases $\Gamma = 4/3$, $z_c = 0$, $\varpi_{i,\text{in}} = 1.5 \times 10^6 \text{ cm}$, and $r_{\text{out}}/r_{\text{in}} = 3$.

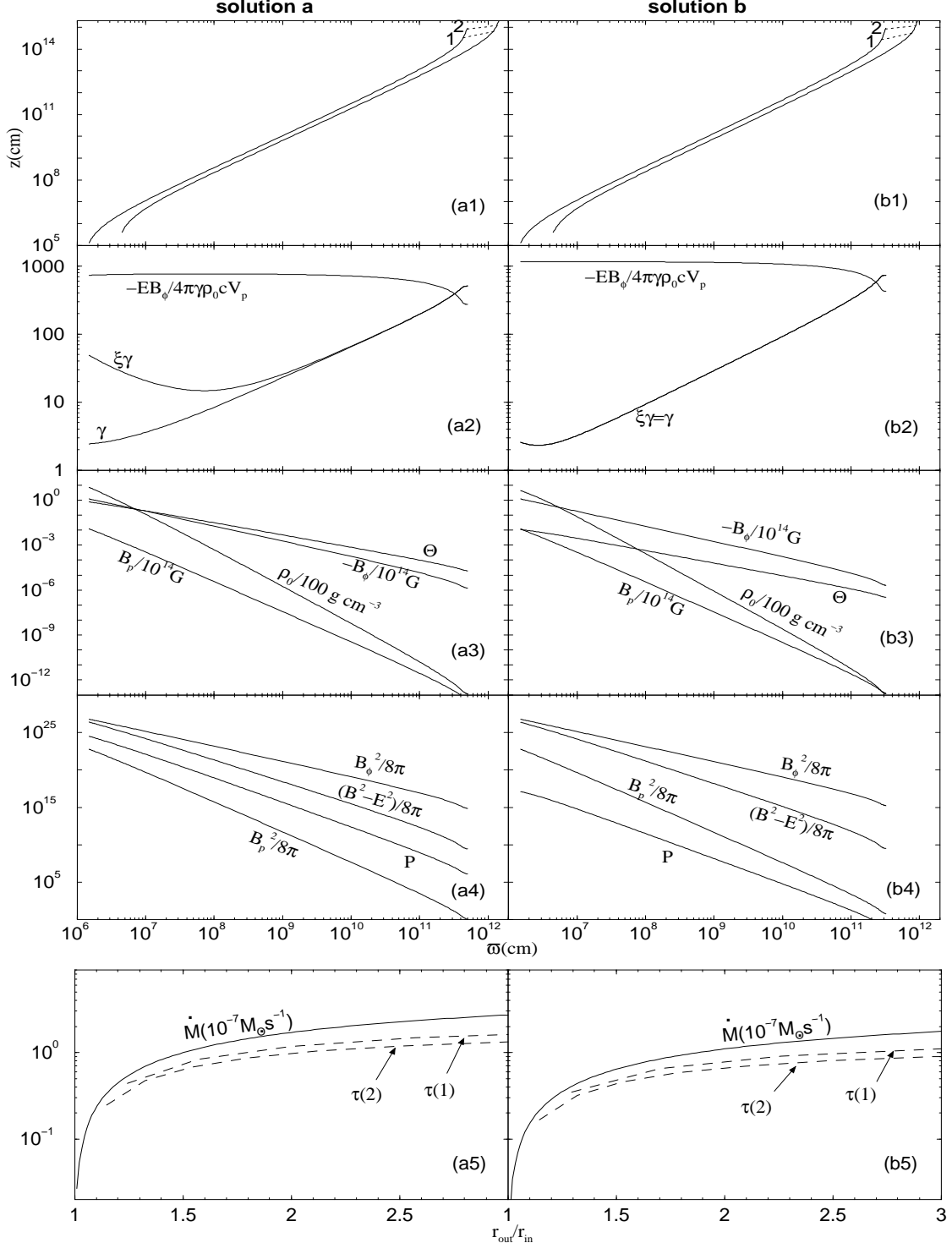


FIG. 1.—Main properties of the two representative solutions discussed in §3. See text for details.

(I.B2d) and (I.B2e). For a specific solution we need to give the value of the model parameter F and seven boundary conditions at the base of the flow. The latter could be, for example, the values of $\Theta_i, \rho_{0i}, B_{pi}, B_{\phi i}, \vartheta_i, V_{pi}, V_{\phi i}$ at the point (r_i, θ_i) where the innermost fieldline is anchored. (The streamline constants μ, q, σ_M, x_A , and $B_0 \bar{\omega}_0^{2-F}$ can then be inferred from eqs. [I.B7a]–[I.B7c].) The requirement that the outflow cross the modified fast-magnetosonic singular surface imposes a constraint on these boundary conditions: this is found numerically as in Paper I.

3. RESULTS

We present the results of the numerical integration for two representative solutions (labeled *a* and *b*), for which the boundary conditions are given in Table 1. The most important physical quantities are plotted in Figure 1, in which each column corresponds to a given solution. The properties of these solutions are described in detail in the following subsections.

3.1. Solution *a*: A Hot, Fast-Rotator Outflow

This solution is intended to represent a realistic GRB outflow: the total energy initially resides predominantly in the electromagnetic field, but the thermal part is nonnegligible, corresponding to temperatures $\Theta_i \lesssim 1$.

Figure 1a1 shows the meridional projections of the innermost (anchored at $\bar{\omega}_{i,\text{in}} = 1.5 \times 10^6 \text{ cm}$) and outermost (anchored at $\bar{\omega}_{i,\text{out}} = 4.5 \times 10^6 \text{ cm}$) fieldlines. Over much of the flow the line shape is fitted by $(z/10^5 \text{ cm}) \approx 4(\bar{\omega}/10^6 \text{ cm})^{1.48}$, and it becomes cylindrical asymptotically. The dashed lines labeled 1 and 2 represent the optical paths for photons that originate at two points on the innermost streamline. The corresponding optical depths $\tau(1)$ and $\tau(2)$ are shown in Figure 1a5. It is seen that the flow becomes optically thin (with τ decreasing to ~ 1) just before reaching the asymptotic cylindrical regime, corresponding to maximum baryon loading (see Vlahakis & Königl 2001).

Figure 1a2 shows the Lorentz factor γ and the two parts of the energy flux in units of $\gamma \rho_0 c^2 V_p$ (i.e., the mass-flux $\times c^2$): the Poynting contribution $-EB_\phi/4\pi\gamma\rho_0 c V_p$ and the matter contribution $\xi\gamma$. The ratio of these two parts is the magnetization function $\sigma = -EB_\phi/4\pi\xi\gamma^2\rho_0 c V_p$, whereas their sum is a constant: $\mu = \xi\gamma - EB_\phi/4\pi\gamma\rho_0 c V_p$ (see eq. [I.13d]).⁶ All quantities are given as functions of the cylindrical distance $\bar{\omega}$ along the innermost streamline. It is seen that γ increases continuously; for a significant portion of the flow it can be fitted by $\gamma \approx (\bar{\omega}/10^6 \text{ cm})^{0.46}$, and its asymptotic value is $\gamma_\infty \approx 500$. The magnetization function decreases from $\sigma_i \approx 15$ near the disk to $\sigma_\infty \approx 0.5$ asymptotically.

Figure 1a3 shows the poloidal and azimuthal components of the magnetic field ($B_p \propto \bar{\omega}^{-2}$, $B_\phi \propto \bar{\omega}^{-1}$), the temperature ($\Theta \propto \bar{\omega}^{-0.813}$), and the comoving baryon density ($\rho_0 \propto \bar{\omega}^{-2.4}$).

Figure 1a4 shows the thermal pressure (due to radiation and pairs) P , and various electromagnetic pressures. The displayed solution corresponds to the case where $B_p^2/8\pi \ll P \ll B_\phi^2/8\pi$ throughout the flow.

Figure 1a5 shows the radial profile of the mass-loss rate. For $\bar{\omega}_{i,\text{out}}/\bar{\omega}_{i,\text{in}} = r_{\text{out}}/r_{\text{in}} = 3$, $M \approx 2.7 \times 10^{-7} M_\odot \text{ s}^{-1}$, corresponding to a total ejected baryonic mass of $M_b \approx 2.7 \times 10^{-6} M_\odot$ for a typical burst duration of $\Delta t \approx 10 \text{ s}$, and to a total injected energy $\mathcal{E}_i = \mu M_b c^2 \approx 3.5 \times 10^{51} \text{ ergs}$. A fraction $(1 + \sigma_\infty)^{-1} \approx 66.7\%$

of \mathcal{E}_i is converted asymptotically into baryon kinetic energy $E_k = \gamma_\infty M_b c^2 \approx 2.3 \times 10^{51} \text{ ergs}$ of the two oppositely directed jets (see eq. [20] below).

3.1.1. Collimation

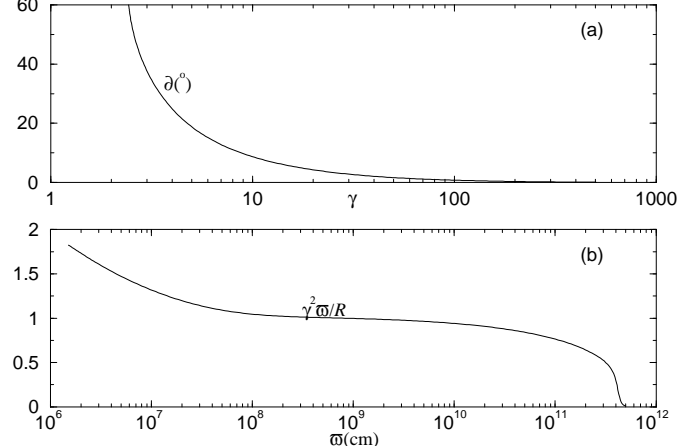


FIG. 2.— (a) Opening half-angle of the jet as a function of the Lorentz factor. (b) The quantity $\gamma^2 \bar{\omega} / R$ (where R is the poloidal curvature radius) as a function of $\bar{\omega}$. Both figures correspond to solution *a*.

It is generally much more difficult to achieve collimation in the case of relativistic flows than in the nonrelativistic case, both because the electric force is as large as the transverse magnetic force and almost cancels it (e.g., Chiueh, Li, & Begelman 1998; Vlahakis 2003) and because the effective matter inertia is larger (e.g., Bogovalov 2001). However, for a flow that is ejected with a mildly relativistic velocity, the bulk of the collimation can take place before it becomes extremely relativistic. Figure 2a shows that most of the collimation in the displayed solution happens near the disk: the flow starts with $\vartheta_i = 60^\circ$ and $\gamma_i = 2.4$ at $\bar{\omega}_{i,\text{in}} = 1.5 \times 10^6 \text{ cm}$, but by $\bar{\omega} \approx 10^8 \text{ cm}$, where $\gamma \approx 10$, it is already collimated to $\vartheta \approx 10^\circ$. The collimation is completed at larger values of γ , and the streamlines eventually become cylindrical. Figure 2b shows that for $\bar{\omega} \gtrsim 10^8 \text{ cm}$ (corresponding to $\gamma \gtrsim 10$) and up to $\bar{\omega} \approx 10^{11} \text{ cm}$ (where the cylindrical regime commences), the quantity $\gamma^2 \bar{\omega} / R$ is approximately constant (Chiueh et al. 1998; see also § 4). Despite the large value of the curvature radius, it is still possible for the opening half-angle to vanish asymptotically.

The collimation is the result of the interplay between the magnetic and electric forces in the transfield direction. Figure 3b shows all the force components in that direction. It is seen that both $\mathbf{f}_{E\perp}$ and $\mathbf{f}_{B\perp}$ change sign (at $\bar{\omega} \approx 5 \times 10^6 \text{ cm}$ and $7 \times 10^6 \text{ cm}$, respectively). In a small region very close to the origin $\mathbf{f}_{E\perp} > 0$ (corresponding to a positive charge density, $J^0 > 0$) and $\mathbf{f}_{B\perp} < 0$ (corresponding to the return-current regime $J_\parallel > 0$). In this region the electric force collimates and the magnetic force acts to decollimate the flow. At larger distances $\mathbf{f}_{E\perp} < 0$ (the charge density becomes negative, $J^0 < 0$) and $\mathbf{f}_{B\perp} > 0$ (corresponding to the current-carrying regime $J_\parallel < 0$). Beyond $\bar{\omega} \approx 10^8 \text{ cm}$ these two forces become almost equal (their difference is the much smaller force $-\mathbf{f}_{I\perp}$), and the collimation continues slowly.

⁶ This constant may, however be different for different shells, i.e., $\mu = \mu(s)$.

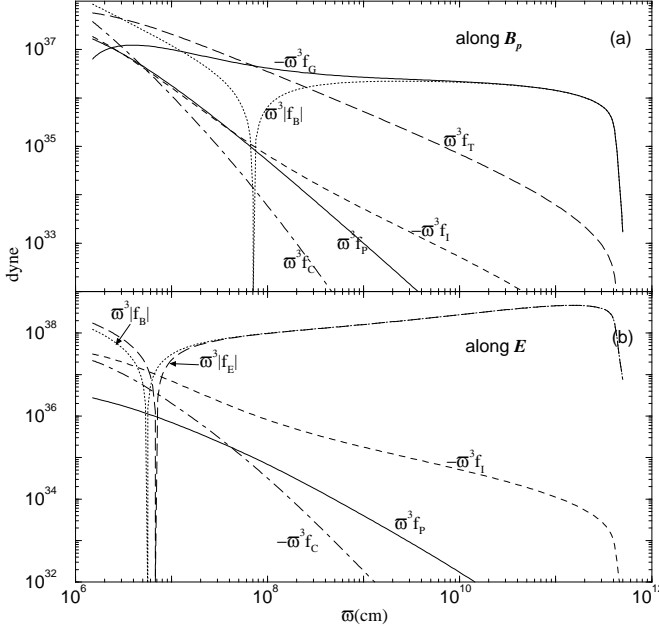


FIG. 3.— Force densities (multiplied by ω^3) along the poloidal flow (top curve) and in the transfield direction (bottom curve), as functions of ω along the innermost streamline of solution *a*. The various force components are defined in eq. (L18).

3.1.2. Acceleration

The poloidal force components along the flow are depicted in Figure 3a. Referring also to Figure 1a2, we identify three different regimes (as in the corresponding trans-Alfvénic solution described in § I.4.1):

1. Thermal acceleration region

For $\omega \lesssim 3 \times 10^8$ cm, the thermal force exceeds the magnetic force, $\mathbf{f}_{T\parallel} > \mathbf{f}_{B\parallel}$. The acceleration is thermal: the increase in γ is caused by the decrease in the specific enthalpy ξ .⁷ A new feature of this solution (not encountered in the corresponding trans-Alfvénic solution presented in Paper I) is that part of the enthalpy flux in this regime is transformed into Poynting flux: for $\omega < 7 \times 10^7$ cm the $\mathbf{f}_{B\parallel}$ component is negative (corresponding to $J_\perp < 0$), resulting in an increase in the Poynting flux and a decrease in the enthalpy flux (see Fig. 1a2). (In the corresponding regime of solution *a* of Paper I, the enthalpy flux $\propto \xi\gamma$ remains constant.) The magnetization function increases from $\sigma \approx 15$ near the disk to $\sigma \approx 50$ at $\omega \approx 7 \times 10^7$ cm, before starting to decrease in the regime where $\mathbf{f}_{B\parallel} > 0$. Combining the conservation relations for the total specific angular momentum and the total specific energy (eqs. [I.13c] and [I.13d]), we get

$$\frac{\Omega}{c^2} \omega V_\phi = 1 + (x_A^2 - 1) \frac{\mu}{\xi\gamma}. \quad (4)$$

Note that for the adopted fiducial values the quantity

$$x_A^2 - 1 = \frac{xM^2}{M^2 + x^2 - xV_\phi/c} \left(\frac{V_\phi}{c} - \frac{B_p}{E} \right)$$

is positive (in contrast to the trans-Alfvénic case, where $x_A^2 < 1$). Thus, equation (4) implies that $\xi\gamma$ decreases with increasing ωV_ϕ . This explains the behavior of $\xi\gamma$ near the base of the flow and indicates when this effect would be most pronounced: it may be expected that ωV_ϕ would increase faster for a larger

⁷ There is a very small region near the origin where $-\mathbf{f}_G$ is small, meaning that the Lorentz factor remains constant (see also Fig. 1a2). However, even though V^2 remains constant, the poloidal velocity increases (while V_ϕ decreases).

initial opening half-angle ϑ_i , so that the region where $\mathbf{f}_{B\parallel} < 0$ would be more extended in this case.

2. Magnetic acceleration region

From the end of the thermal acceleration zone, where $\xi \approx 1$, up to $\omega \approx 4 \times 10^{11}$ cm, it is seen from Figure 1a2 that the Lorentz factor continues to increase. The acceleration in this regime is due to magnetic effects: Poynting flux is transformed into kinetic energy flux. Figure 3a shows that the force $-\mathbf{f}_{G\parallel}$ (which measures the increase in γ) is equal to the magnetic force $\mathbf{f}_{B\parallel}$ (which derives from the decrease in $|\omega B_\phi|$).

Even though $\omega/\mathcal{R} \lesssim 1/\gamma^2$ (see Fig. 2b), in agreement with the analysis of Chiueh et al. (1998), their argument that no significant acceleration can take place at large distances from the light cylinder is evidently circumvented in this case: the σ function in the magnetic acceleration region decreases from $\sigma \approx 50$ to the asymptotic value $\sigma_\infty \approx 0.5$. This behavior is explained in Vlahakis (2003), who analyzes the efficiency of magnetic acceleration in relation to the fieldline shape and the role of the centrifugal force in the transfield force-balance equation. As the flow becomes progressively more matter-dominated, an important transition is reached (at $\sigma = \sigma_c$) when the centrifugal force becomes equal to the electromagnetic force component in the transfield direction. The acceleration could in principle continue beyond that point only if a transition from a positive to a negative poloidal curvature were possible. This cannot happen in r self-similar models, which therefore have $\sigma_\infty \leq \sigma_c$. Large asymptotic cylindrical radii correspond to a comparatively smaller centrifugal force and therefore, (on account of $\mathbf{f}_{B\perp} + \mathbf{f}_{E\perp} = -\mathbf{f}_{C\perp}$) to a less magnetized asymptotic flow. This explains why the super-Alfvénic solutions presented in this paper attain smaller values of σ_∞ than the corresponding solutions of Paper I, which generally collimate more efficiently than super-Alfvénic flows.

3. Asymptotic cylindrical region

At the end of the magnetic acceleration region the flow becomes cylindrical: Figure 1a1 shows that the fieldlines converge to a constant value of ω and that subsequently all the flow quantities remain constant.

3.1.3. Time-Dependent Effects

The disk activity that determines the time variability of a GRB remains an open question, so one is not yet in a position to accurately specify the time profile of the boundary conditions at the base of the flow. We nevertheless present in this subsection an illustrative example of how one may recover the time dependence imprinted on the flow by the s dependence of the boundary conditions at the origin. In particular, we show how to obtain the function $\gamma(\ell, s)$ [or, using $s = ct - \ell$, the function $\gamma(\ell, t)$; see also § I.4.1.1].

Equations (A1d) and (A1f) give

$$\gamma(\ell, s) = \gamma(\ell, s_0) \frac{\mu(s)}{\mu(s_0)} \frac{\xi(\ell, s_0)}{\xi(\ell, s)} \quad (5)$$

and

$$\frac{\xi(\ell, s)}{[\xi(\ell, s) - 1]^3} = \frac{g(s)}{g(s_0)} \frac{q(s_0)}{q(s)} \frac{\xi(\ell, s_0)}{[\xi(\ell, s_0) - 1]^3}. \quad (6)$$

For given $g(s)$, $g(s)/\mu(s)$, $q(s)$ and a known solution $\{\xi(\ell, s_0), \gamma(\ell, s_0)\}$ for the reference shell s_0 , we can solve this system of equations to obtain $\{\xi(\ell, s), \gamma(\ell, s)\}$ for all the other shells of the outflow.

As a concrete example, we choose the functions $g(s)$ and $g(s)/\mu(s)$ as shown in the inset of Figure 4. In the context of the internal-shock model of GRBs, these functions can be interpreted as the envelope profiles of a series of discrete pulses. Since the Poynting flux is $\propto g(s)$, we choose $g_{\max}/g_{\min} = 10^4$, corresponding to an azimuthal magnetic field amplification factor $B_{\phi \max}/B_{\phi \min} = 10^2$. The profile of $g(s)/\mu(s) \propto \gamma \rho_0$ is similar to the one adopted in Paper I. We also set $g(s) \propto g(s)\mu^2(s)$, for which choice the solution of equations (5) and (6) near the origin (where $\xi \gg 1$) is $\gamma(\ell \approx 0, s) \approx \gamma(\ell \approx 0, s_0)$.⁸ The resulting Lorentz factor profile $\gamma(\ell, t)$ is shown in Figure 4.

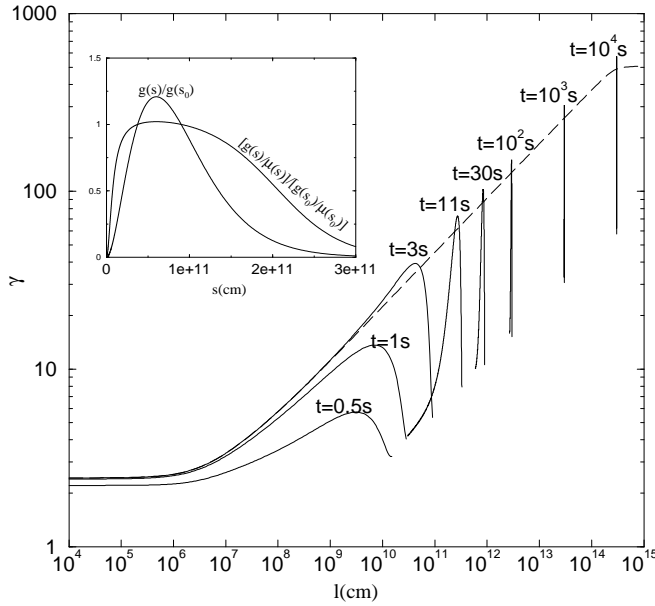


FIG. 4.— Lorentz factor plotted as a function of the arclength along the innermost fieldline of solution *a* for several values of time since the start of the burst. The dashed line represents the “time independent” solution for the reference shell $s_0 = 0.9 \times 10^{11}$ cm. The assumed forms of the functions $g(s)$ and $g(s)/\mu(s)$ across the ejected “pancake” are shown in the inset.

For $t = 0.5$ s, only the shells with $s \in [0, ct = 1.5 \times 10^{10}$ cm] have been ejected. The ejecta occupy the region from $\ell = 0$ to $\ell = ct = 1.5 \times 10^{10}$ cm, and the first shells have already been accelerated.

At time $t = 11$ s, the whole “pancake” $s \in [0, c\Delta t = 3 \times 10^{11}$ cm] can be seen (assuming a typical duration of $\Delta t = 10$ s). It occupies the region $\ell \in [ct - c\Delta t = 3 \times 10^{10}$ cm, $ct = 3.3 \times 10^{11}$ cm].

The acceleration continues and at $t = 10^4$ s the asymptotic stage is reached. Although the shells were ejected with the same γ_i , they now span a wide range of Lorentz factors [corresponding to the linear dependence $\gamma_\infty(s) = (\sigma_\infty + 1)^{-1} \mu(s)$], which would have the effect of enhancing the emission efficiency of the resulting internal shocks (e.g., Kobayashi, Piran, & Sari 1997).

3.2. Solution *b*: The Cold Case ($\xi_i \approx 1$)

The cold solution presented in the second column of Figure 1 is more magnetized than solution *a*: the initial value of its magnetization function is $\sigma_i \approx 450$. As a result, it collimates faster and the asymptotic jet radius ϖ_∞ is smaller than the corresponding radius in the fiducial solution.

⁸ For these forms of the s dependence, we verified that the neglected terms in the momentum equation (I.12e) are very small compared with the other terms of that equation.

The asymptotic baryon kinetic energy is the same as in solution *a*, and the baryon loading is similarly the maximum allowed under the condition that the flow be optically thin in the asymptotic regime ($\tau_\infty \approx \sigma_T \varpi_\infty \rho_0 \infty / m_p \approx 1$). Since $E_k \propto \rho_0 \infty \gamma_\infty^2 \varpi_\infty^2 \Delta t \propto \tau_\infty \gamma_\infty^2 \varpi_\infty$, the smaller asymptotic jet radius implies a larger value of γ_∞ (and hence a smaller baryonic mass). The actual numbers for solution *b* are $\dot{M} \approx 1.75 \times 10^{-7} M_\odot$ s⁻¹, $\gamma_\infty \approx 730$ (corresponding to $\sigma_\infty \approx 0.58$), and an acceleration efficiency $E_k/\mathcal{E}_i = (1 + \sigma_\infty)^{-1} \approx 63.3\%$. In this case $P \ll B_p^2/8\pi \ll B_\phi^2/8\pi$ throughout the flow.

Figure 1b2 shows a slight initial decrease in $\xi \gamma \approx \gamma$. This behavior is similar to the one exhibited by solution *a* and again corresponds to a negative value of $\mathbf{f}_{B\parallel}$. In this case, however, the Poynting flux increases not at the expense of the thermal energy but rather because a fraction of the kinetic energy of rotational motion is transformed into electromagnetic energy (with the remainder of the rotational energy accounting for the increase in the kinetic energy of poloidal motion in this region).

4. DISCUSSION

The outflow solutions depicted in Figure 1 exhibit a power-law behavior over most of their extent. We now show that these power-law scalings can be obtained analytically.

The Bernoulli equation implies $V_p \approx c$, or, using equation (A1c),

$$\frac{F\sigma_M}{\mu} \frac{\sin \theta}{\sin(\theta-\vartheta)} \frac{\mathcal{X}^2 + \mathcal{M}^2}{\mathcal{X}^2} \approx 1. \quad (7)$$

Well above the disk surface (where $\theta, \vartheta \ll \pi/2$ and $\xi \approx 1$), equation (7) yields

$$\left(\frac{d \ln \varpi}{d \ln z} \right)_A = \frac{\vartheta}{\theta} = 1 - \frac{F\sigma_M}{\mu} \left(1 + \frac{1}{\sigma} \right), \quad (8)$$

where we approximated the magnetization function $\sigma = -(cEB_\phi/4\pi)/(\xi \gamma^2 \rho_0 c^2 V_p)$ by $\mathcal{X}^2/\mathcal{M}^2$. In the Poynting flux-dominated regime $\sigma \gg 1$, so the fieldline shape is

$$z \propto \varpi^{\frac{\mu}{\mu - F\sigma_M}}. \quad (9)$$

The opening half-angle $\vartheta \propto \varpi^{-F\sigma_M/(\mu - F\sigma_M)}$, and the curvature radius satisfies

$$\frac{\varpi}{\mathcal{R}} = -\varpi \frac{\partial^2 \varpi(z, A)}{\partial z^2} \left(\frac{B_z}{B_p} \right)^3 \approx \frac{F\sigma_M}{\mu} \left(1 - \frac{F\sigma_M}{\mu} \right) \frac{\varpi^2}{z^2}. \quad (10)$$

The transfield force-balance equation can be written as

$$\frac{\varpi \nabla_s A}{|\nabla_s A|} \cdot \nabla_s \ln \left| \frac{\varpi B_\phi}{\gamma} \right| \approx \gamma^2 \frac{\varpi}{\mathcal{R}} \frac{B_p^2}{B_\phi^2} (M^2 + x^2) \quad (11)$$

(e.g., Chiueh et al. 1991; Okamoto 2002; Vlahakis 2003). Using $x^2/M^2 \approx \sigma \gg 1$, $-B_\phi \approx E = xB_p$, and assuming that $-\varpi B_\phi/\gamma = A^m \mathcal{F}(\ell)$ (a form verified by numerical integration at least in the current-carrying regime), we get

$$\gamma^2 \frac{\varpi}{\mathcal{R}} = m \frac{\varpi |\nabla_s A|}{A}. \quad (12)$$

From the definition of the fieldline constant σ_M ($= A\Omega^2/\Psi_A c^3$) and the fact that the flow is Poynting flux-dominated ($\mu \approx -\varpi \Omega B_\phi/\Psi_A c^2$) we obtain

$$\frac{\varpi |\nabla_s A|}{A} = \frac{\mu}{\sigma_M}, \quad (13)$$

so equation (12) yields

$$\gamma^2 \frac{\varpi}{\mathcal{R}} = m \frac{\mu}{\sigma_M}. \quad (14)$$

Figure 2b verifies that the right-hand side is a constant (≈ 1). Equation (10) then implies

$$\gamma \approx \frac{\mu}{F\sigma_M} \left(\frac{mF}{1-F\sigma_M/\mu} \right)^{1/2} \frac{z}{\varpi}, \quad (15)$$

i.e.,

$$\gamma \propto \varpi^\beta, \quad \beta = \frac{F\sigma_M}{\mu - F\sigma_M}, \quad \text{and} \quad \gamma \propto z^{(F\sigma_M/\mu)}. \quad (16)$$

The scaling $\gamma \propto z/\varpi$ can also be derived from kinematic considerations: $d\varpi \sim V_\varpi dt \sim (c^2 - V_z^2)^{1/2} dt$, and for $V_\varpi \ll V_z$ we get $\gamma \sim dz/d\varpi \propto z/\varpi$ for a fieldline shape of the form of equation (9).

The solutions derived in §3 have $\beta \approx 0.46$ and 0.49 in the “hot” and “cold” cases, respectively. The other scalings are easier to derive: using equation (13) we get

$$B_p \approx \frac{\mu A}{\sigma_M} \varpi^{-2}, \quad B_\phi \approx -xB_p \approx -\frac{\mu A \Omega}{c\sigma_M} \varpi^{-1}. \quad (17)$$

Note that it is, in fact, the deviation from the last two scaling relations that gives rise to the acceleration:

$$\frac{\mu A \Omega}{c\sigma_M} + \varpi B_\phi = \frac{A \Omega}{c\sigma_M} \gamma \propto \varpi^\beta \quad (18)$$

(where we used the definition [I.13d] of μ in the limit $\xi \simeq 1$). Finally, from the constancy of the mass-to-magnetic flux ratio and from the polytropic relation we infer

$$\gamma \rho_0 \approx \frac{\Psi_A \mu A}{4\pi c \sigma_M} \varpi^{-2}, \quad \Theta \propto \rho_0^{1/3} \propto \varpi^{-(\beta+2)/3}. \quad (19)$$

The fiducial “hot” trans-Alfvénic solution presented in Paper I also exhibits a power-law behavior. Its power-law exponents can be obtained as a special case ($\beta = 1$) of the preceding results, corresponding to a parabolic fieldline shape ($z \propto \varpi^2$) and $\gamma \propto \varpi$ (see Vlahakis & Königl 2001). As demonstrated above, our fiducial super-Alfvénic flow accelerates significantly more slowly with distance from the source.

Equation (8) shows that, as the flow accelerates and the value of the magnetization function declines, the jet opening half-angle decreases faster than θ . The cylindrical regime is thus reached at a finite distance from the source, corresponding to

$$\sigma_\infty = \frac{F\sigma_M}{\mu - F\sigma_M}, \quad \gamma_\infty = \frac{\mu}{1 + \sigma_\infty} = \mu - F\sigma_M, \quad (20)$$

which yield an acceleration efficiency $E_k/\mathcal{E}_i = \gamma_\infty/\mu = (1 + \sigma_\infty)^{-1} = 1 - F\sigma_M/\mu$. Higher efficiencies thus correspond to larger values of $\mu/F\sigma_M$. We can use equation (A1c) to relate this parameter combination to the boundary conditions at the base of the flow: $\mu/F\sigma_M = c \sin \theta_i / V_{p,i} \sin(\theta_i - \vartheta_i)$, or, for $\theta_i \approx \pi/2$, $\mu/F\sigma_M \approx c/V_{z,i}$. The poloidal velocity cannot be very small ($V_{p,i} \approx -E/B_\phi$ should be close to 1 to allow the flow to reach large distances; see § 2), so a high efficiency requires a large initial opening half-angle ϑ_i . However, a large value of $\mu/F\sigma_M$ also implies a small value of the exponent $\beta = d \ln \gamma / d \ln \varpi$, and since γ_∞ is always close to μ , $\varpi_\infty \approx \varpi_i \mu^{1/\beta}$ would have to be large. Since $z \propto \varpi^{1+\beta}$, this places a practical upper limit on ϑ_i : it cannot be too large or else the acceleration would be completed on scales much larger than typically inferred for GRB outflows ($\sim 10^{14} - 10^{15}$ cm).

Drenkhahn & Spruit (2002) examined a pure- B_ϕ , strictly radial flow without considering the transfield force-balance equation. They showed that magnetic energy dissipation (modeled in a parameterized manner) results in efficient acceleration $\gamma \propto r^{0.25}$ and a final Poynting-to-kinetic energy conversion efficiency $\approx 54\%$. Our fiducial solution exhibits a faster acceleration $\gamma \propto r^{0.31}$ and a higher efficiency $\approx 67\%$. These results indicate that both dissipation and the fieldline shape may play an important role in the flow acceleration.

5. CONCLUSION

Using the radially self-similar relativistic MHD model presented in Paper I, we constructed representative “hot” and “cold” fast-rotator solutions of super-Alfvénic flows. We argued that super-Alfvénic outflows in which $|B_\phi/B_p| \gg 1$ already at the source could plausibly arise in GRB source models that invoke differential rotation in a disk or a star to account for the large magnetic field amplitudes that are required for consistency with the observations. We demonstrated that our “frozen pulse” formulation, despite being quasi steady, can still capture the expected time-variability of the azimuthal field component at the source. We showed that for typical source parameters the flows convert Poynting flux to kinetic-energy flux with high efficiency ($\approx 67\%$ for our fiducial solution) and collimate to cylindrical structures on scales $\gtrsim 10^{14}$ cm. Our solutions confirm (some previous statements in the literature notwithstanding) that significant magnetic acceleration and collimation can take place at large distances from the source (well beyond the light cylinder), although most of the collimation is achieved before the flow becomes extremely relativistic.

The super-Alfvénic solutions derived in this paper are distinguished from the trans-Alfvénic ones obtained in paper I in two main respects: (1) During the initial thermal-acceleration phase of the “hot” solution, some of the internal energy is transformed into electromagnetic energy even as another part is used to increase the poloidal velocity. (The same behavior is exhibited by the “cold” solution, except that in that case the energy reservoir is the bulk initial rotation rather than the thermal energy.) (2) During the subsequent magnetic-acceleration phase, the rate of increase of the Lorentz factor with distance from the source can be significantly lower than in the trans-Alfvénic case; the rate of increase of the jet radius with distance is correspondingly higher. Overall, however, the two types of solution are quite similar, and we derived analytic scaling relations that describe them both (see also Vlahakis & Königl 2001). We conclude that source configurations with either $|B_p/B_\phi| \gtrsim 1$ or $|B_p/B_\phi| \ll 1$ could in principle produce viable GRB outflows. Another potentially important aspect of such outflows, namely, the possibility that their initial composition is highly neutron-rich, can also be modeled within the theoretical framework that we have constructed. This is discussed in a separate publication (Vlahakis et al. 2003).

This work was supported in part by NASA grant NAG5-12635 and by the U.S. Department of Energy under grant B341495 to the Center for Astrophysical Thermonuclear Flashes at the University of Chicago. N. V. also acknowledges support from a McCormick Fellowship at the Enrico Fermi Institute.

APPENDIX

A. PHYSICAL QUANTITIES

In the super-Alfvénic regime ($M^2 \gg 1 - x^2, x \gg x_A$) of the r self-similar model described in Paper I, the expressions for the various physical quantities as functions of r, θ , and $s \equiv ct - \ell$ take the form:

$$\mathbf{B} = \frac{B_0(s_0)\varpi_0^{2-F}(s_0)x_A^F(s_0)}{g^{F/2}(s_0)} \left[\frac{(r \sin \theta)^{F-1}}{\mathcal{X}^F r \sin(\theta - \vartheta)} (\hat{z} \cos \vartheta + \hat{\omega} \sin \vartheta) - \frac{\mu(s_0)}{\sigma_M(s_0)} \frac{(r \sin \theta)^{F-2} g^{1/2}}{F \mathcal{X}^{F-3} (\mathcal{X}^2 + \mathcal{M}^2)} \hat{\phi} \right], \quad (\text{A1a})$$

$$\mathbf{E} = \frac{B_0(s_0)\varpi_0^{2-F}(s_0)x_A^F(s_0)}{g^{F/2}(s_0)} \frac{(r \sin \theta)^{F-2} \sin \theta g^{1/2}}{\mathcal{X}^{F-1} \sin(\theta - \vartheta)} (\hat{z} \sin \vartheta - \hat{\omega} \cos \vartheta), \quad (\text{A1b})$$

$$\frac{\mathbf{V}}{c} = \frac{F \sigma_M(s_0)}{\mu(s_0)} \frac{\sin \theta}{\sin(\theta - \vartheta)} \frac{\mathcal{X}^2 + \mathcal{M}^2}{\mathcal{X}^2} (\hat{z} \cos \vartheta + \hat{\omega} \sin \vartheta) + \frac{x_A^2(s)}{\mathcal{X} g^{1/2}} \hat{\phi}, \quad (\text{A1c})$$

$$\xi \gamma = \mu(s) \frac{\mathcal{M}^2}{\mathcal{X}^2 + \mathcal{M}^2}, \quad (\text{A1d})$$

$$\gamma \rho_0 = \left(\frac{B_0(s_0)\varpi_0^{2-F}(s_0)x_A^F(s_0)}{g^{F/2}(s_0)} \right)^2 \frac{\mu(s_0)}{\sigma_M(s_0)} \frac{g(s)}{\sigma_M(s)} \frac{(r \sin \theta)^{2(F-2)}}{4\pi c^2 F^2 \mathcal{X}^{2(F-2)} (\mathcal{X}^2 + \mathcal{M}^2)}, \quad (\text{A1e})$$

where $x^2 = \mathcal{X}^2 g(s)$, $M^2 = \mathcal{M}^2 g(s)$, $\frac{B_0(s)\varpi_0^{2-F}(s)x_A^F(s)}{g^{F/2}(s)} = \frac{B_0(s_0)\varpi_0^{2-F}(s_0)x_A^F(s_0)}{g^{F/2}(s_0)}$, $\mu(s) = \sigma_M(s) \frac{\mu(s_0)}{\sigma_M(s_0)}$, and the functions $g(s)$, $x_A(s)$, $\sigma_M(s)$, and $q(s)$ can be specified freely. The functions $\mathcal{X}^2(\theta)$, $\mathcal{M}^2(\theta)$, and $\vartheta(\theta)$ can be found from the integration of the ordinary differential equations (I.B2d) and (I.B2e) of Paper I, whereas ξ is given from

$$\frac{\xi}{(\xi - 1)^{\frac{1}{F-1}}} = \frac{g(s)}{q(s)} \mathcal{M}^2. \quad (\text{A1f})$$

REFERENCES

Abbott, W. P., & Fisher, G. H. 2003, *ApJ*, 582, 475
 Akiyama, S., Wheeler, J. C., Meier, D., & Lichtenstadt, I. 2003, *ApJ*, 584, 954
 Balbus, S. A., & Hawley, J. F. 1998, *Rev. Mod. Phys.*, 70, 1
 Bogovalov, S. V. 2001, *A&A*, 371, 1155
 Brummell, N., Cline, K., & Cattaneo, F. 2002, *MNRAS*, 329, L73
 Cao, X., & Spruit, H. C. 1994, *A&A*, 287, 80
 Chakrabarti, S. K., & D'Silva, S. 1994, *ApJ*, 424, 138
 Chiueh, T., Li, Z.-Y., & Begelman, M.C. 1991, *ApJ*, 377, 462
 Chiueh, T., Li, Z.-Y., & Begelman, M.C. 1998, *ApJ*, 505, 835
 Contopoulos, J. 1995, *ApJ*, 450, 616
 Coroniti, F. V. 1981, *ApJ*, 244, 587
 Drenkhahn, G., & Spruit, H. C. 2002, *A&A*, 391, 1141
 Eardley, D. M., & Lightman, A. P. 1975, *ApJ*, 200, 187
 Fryer, C. L. 1999, *ApJ*, 522, 413
 Haswell, C. A., Tajima, T., & Sakai, J.-I. 1992, *ApJ*, 401, 495
 Klužniak, W., & Ruderman, M. 1998, *ApJ*, 505, L113
 Kobayashi, S., Piran, T., & Sari, R. 1997, *ApJ*, 490, 92
 Lee, H. K., Wijers, R. A. M. J., & Brown, G. E. 2000, *Phys. Rep.*, 325, 83
 Lyutikov, M., & Blandford, R. 2002, preprint (astro-ph/0210671)
 MacFadyen, A. I., & Woosley, S. E. 1999, *ApJ*, 524, 262
 MacFadyen, A. I., Woosley, S. E., & Heger, A. 2001, *ApJ*, 550, 410
 Mészáros, P., & Rees, M. J. 1997, *ApJ*, 482, L29
 Miller, K. A., & Stone, J. M. 2000, *ApJ*, 534, 398
 Okamoto, I. 2002, *ApJ*, 573, L31
 Ruderman, M. A., Tao, L., & Klužniak, W. 2001, *ApJ*, 542, 243
 Shibata, K., Tajima, T., & Matsumoto, R. 1990, *ApJ*, 350, 295
 Stella, L., & Rosner, R. 1984, *ApJ*, 277, 312
 Thompson, C., & Murray, N. 2001, *ApJ*, 560, 339
 Vietri, M., & Stella, L. 1998, *ApJ*, 507, L45
 Vlahakis, N. 2003, *ApJ*, submitted
 Vlahakis, N., Peng, F., & Königl, A. 2003, *ApJ*, to be submitted
 Vlahakis, N., & Königl, A. 2001, *ApJ*, 563, L129
 Vlahakis, N., & Königl, A. 2003, *ApJ*, submitted, preprint astro-ph/0303482
 (Paper I)